The desmoplakin/intermediate filament linkage regulates cell mechanics

Joshua A. Broussard[b,f+], Ruiguo Yang[a+], Changjin Huang[a], S. Shiva P. Nathamgari[a], Allison M. Beese[a], Lisa M. Godsel[b,f], Marihan H. Hegazy[b], Sherry Lee[b], Fan Zhou[a], Nathan J. Sniadecki[c,d,e], Kathleen J. Green[*,b,f], and Horacio D. Espinosa[*,a,g]

[a]Department of Mechanical Engineering, Northwestern University, Evanston, IL 60208

[b]Department of Pathology, Northwestern University, Feinberg School of Medicine, Chicago, IL 60611

Departments of [c]Mechanical Engineering and [d]Bioengineering, [e]Institute for Stem Cell and Regenerative Medicine, University of Washington, Seattle, WA 98195

[f]Department of Dermatology, Northwestern University, Feinberg School of Medicine, Chicago, IL 60611

[g]Theoretical and Applied Mechanics Program, Northwestern University, Evanston, IL 60208

[*]To whom correspondence should be addressed. Email: K. J. G. (kgreen@northwestern.edu) or H. D. E. (espinosa@northwestern.edu).

+These authors contributed equally.

Running Head: Desmosomes regulate cell mechanics

Abbreviations: MA, micropillar arrays; AFM, atomic force microscopy; DSM, desmosome; DP, desmoplakin; DPNTP, desmoplakin n-terminal polypeptide; IF, intermediate filaments; PDMS, polydimethylsiloxane; Wt, wild type.

Total number of characters: 19,882

Abstract

The translation of mechanical forces into biochemical signals plays a central role in guiding normal physiological processes during tissue development and homeostasis. Interfering with this process contributes to cardiovascular disease, cancer progression, and inherited disorders. The actin-based cytoskeleton and its associated adherens junctions are well-established contributors to mechanosensing and transduction machinery; however, the role of the desmosome/intermediate filament network is poorly understood in this context. Because a force balance among different cytoskeletal systems is important to maintain normal tissue function, knowing the relative contributions of these structurally integrated systems to cell mechanics is critical. Here, we modulated the interaction between desmosomes and intermediate filaments using mutant forms of desmoplakin, the protein bridging these structures. Using micropillar arrays and atomic force microscopy, we demonstrate that strengthening the desmosome/intermediate filament interaction increased cell-substrate and cell-cell forces and cell stiffness both in cell pairs and sheets of cells. In contrast, disrupting the interaction leads to a decrease in these forces. These alterations in cell mechanics are abrogated when the actin cytoskeleton is dismantled. These data suggest that the tissue-specific variability in desmosome/intermediate filament network composition provides an opportunity to differentially regulate tissue mechanics by balancing and tuning forces among cytoskeletal systems.

Introduction

Cells are integrated into tissues through macromolecular adhesive organelles specialized for anchoring different cytoskeletal components at cell-extracellular matrix and cell-cell adhesion sites. At the cell substrate, actin and intermediate filaments (IF) are anchored by focal adhesions and hemidesmosomes, respectively, whereas at cell-cell interfaces, actin and IF are anchored by adherens junctions (AJs) and desmosomes (DSMs) (Simpson *et al.*, 2011). Under physiological conditions, these adhesion/cytoskeletal systems are highly integrated, and mechanical forces produced by individual cells are disseminated throughout a tissue by means of this cohesive network. The resulting mechano-chemical coupling is required for tissue morphogenesis, collective cell migration, as well as cell proliferation and differentiation (DuFort *et al.*, 2011; Eyckmans *et al.*, 2011). Moreover, a number of pathological conditions and developmental disorders result from aberrant mechanical cues, including arthritis, atherosclerosis, and cancer (Jaalouk and Lammerding, 2009).

Cells within tissues exist in a "prestressed" condition where forces present within their mechanical components are balanced in a state of isometric tension; this has been suggested to be critical for mechanotransduction whereby mechanical forces are translated into biochemical cues (Ingber, 2008). Studies of mechanotransduction have focused primarily on actin-based adhesive organelles. For example, enhanced integrin signaling, resulting from matrix stiffening, promotes tumor progression (Levental *et al.*, 2009), and mechanical tension regulates Yap and β-catenin transcriptional activity through E-cadherin, driving cell cycle entry (Benham-Pyle *et al.*, 2015). Actomyosin contraction is required to generate tension at both cell-cell and cell-substrate adhesions (Aguilar-Cuenca *et al.*, 2014; de Rooij, 2014), and there is cross talk between the mechanical forces at these two interfaces (Maruthamuthu *et al.*, 2011; Mertz *et al.*, 2013; Green *et al.*, 2015). In addition, actin-based AJs have an established role in regulating the emergence of tissue-level tension in cell monolayers (Harris *et al.*, 2014). However, much less is known about the role of the IF-based adhesions in regulating cell-cell and cell-substrate forces. In spite of their well-accepted role in maintaining the mechanical integrity of tissues, IF-based adhesions have been largely ignored with respect to their potential roles in mechanotransduction. Furthermore, though some progress has been made identifying how specific components of the mechanical networks participate in mechanotransduction, how these systems function cooperatively to orchestrate mechanically regulated cell behaviors remains poorly understood.

DSMs are cadherin-based cell adhesions that anchor strain-bearing IF at sites of cell-cell contact (Figure 1A). They are the most prevalent adhesive structure in tissues that undergo considerable mechanical strain, including heart and skin, and DSM perturbations are associated with diseases of these organs (Broussard *et al.*, 2015). We have previously shown that enhancing or disrupting the connection between DSMs and IF qualitatively increases or decreases cell-cell adhesive strength (Bornslaeger *et al.*, 1996; Huen *et al.*, 2002; Hobbs and Green, 2012). However, the contribution of IF-based adhesive networks to cell-cell and cell-substrate forces as well as tissue-level tension is poorly understood.

Several methods for quantitative assessment of cell forces have been developed, including atomic force microscopy (AFM) (Brunner *et al.*, 2006; Prass *et al.*, 2006), traction force microscopy (Maruthamuthu *et al.*, 2011; Legant *et al.*, 2013; Benham-Pyle *et al.*, 2015),

fluorescence microscopy-based tension biosensors (Grashoff *et al.*, 2010; Borghi *et al.*, 2012), optical traps (Galbraith and Sheetz, 1999; Kress *et al.*, 2007), and elastic micropillar arrays (MA) (Tan *et al.*, 2003; Liu *et al.*, 2010; Cohen *et al.*, 2013). These techniques have been used to study cell forces in the context of actin-based adhesive networks, but have not been systematically applied to the study of IF-based adhesive networks. Here, we use both MA and AFM to determine for the first time the contribution of the DSM/IF network to cell stiffness as well as cell-substrate and cell-cell mechanical forces. We demonstrate that modulating the strength of the DSM/IF linkage affects cell forces in the context cell pairs and within larger groups of cells. In addition, our data show that these effects are at least in part mediated through regulation of the actin cytoskeleton and support a model in which the DSM/IF network could act as a compressive element, counterbalancing actomyosin-generated tension.

Results and Discussion

Measuring changes in contractility using MA

Modulating actomyosin contractility has previously been shown to regulate cell forces using MA (Liu *et al.*, 2010). This approach provided us a baseline with which to compare the role of the DSM/IF linkage in regulating cell forces as well as a means of validating our MA system. We generated MA using a process previously described (Yang *et al.*, 2011). Individual pillars had a height of 10 μm and diameter of 2 μm (Supplemental Figure 1A). This resulted in a Young's modulus, as measured by AFM, of 2.41±0.04 MPa. A mixture of fibronectin and fluorescent antibody was transferred onto the tips of the pillars by stamping, enabling cell attachment and pillar tip positioning to quantify displacement (Figure 1B). Cell forces deflect the pillars and can be measured by calculating the pillar displacement compared to a reference position obtained by interpolating the coordinates of unoccupied pillars. Traction forces are then calculated using the measured deflection, considering each pillar as an individual linear elastic mechanical cantilever beam with a tilted base (Schoen *et al.*, 2010; Yang *et al.*, 2011). To account for non-linearity at large deflections, we performed finite element simulations to extract the traction force-displacement relationship of the pillars (Supplemental Figure 1, B and C). A quadratic function was obtained to calculate cell forces: $f_i = 0.1921 s_i^2 + 5.3659 s_i$, where f_i and s_i are the traction force (nN) and lateral deflection of the pillar i (μm). Within a cell pair, the net forces are in equilibrium. Therefore, the sum of the traction forces in one cell is equal and opposite in direction to that of the adjacent cell and vice versa, and thus represents the intercellular force (Liu *et al.*, 2010; Cohen *et al.*, 2013). This force balance was experimentally verified in our system (Figure 1C).

To determine if our system is capable of detecting changes in cell forces, we either inhibited or enhanced cell contractility using the myosin inhibitor blebbistatin or the Rho activator CN01, respectively, and quantified intercellular forces in pairs of epidermoid carcinoma A431 cells as well as traction forces in cell pairs and individual cells. Cell pairs treated with these drugs retained cell-cell contacts and intact actin cytoskeletons (Figure 1D). Blebbistatin led to a significant decrease in the average intercellular tugging force and traction force per pillar (Figure 1E), consistent with a report in endothelial cells (Liu *et al.*, 2010). Decreased cell-substrate forces were observed for both cell pairs and individual cells. However, CN01 resulted in a significant increase in these forces compared with DMSO-treated controls (Figure 1E). These

data suggest that quantification using our MA system is capable of detecting changes in cell-substrate and cell-cell adhesion forces.

The DSM/IF linkage regulates cell forces

To investigate the functional role of DSM/IF network in regulating cell adhesive forces, we utilized inducible A431 stable cell lines expressing various forms of desmoplakin (DP), which provides the physical linkage from the DSM core components to IF. These included wild type (Wt) DP, DPNTP, and S2849G DP (Figure 2A). Doxycycline, which is used to induce protein expression in this cell system, did not affect cell forces (Figure 1E). DPNTP is a DP truncation mutant lacking the IF-binding region of DP and uncouples DSMs from IF (Bornslaeger *et al.*, 1996; Huen *et al.*, 2002) (Figure 2B), while S2849G DP contains a serine to glycine mutation that enhances IF binding by interfering with GSK3β-dependent processive phosphorylation of DP (Meng *et al.*, 1997; Hobbs and Green, 2012; Albrecht *et al.*, 2015) (Figure 2B). Qualitatively, these mutations have been shown to decrease or increase cell-cell adhesion, respectively, but quantitative analysis has not been performed. In addition, the role of DP in regulating cell-substrate adhesion has not been addressed.

To determine if modulating the DSM/IF linkage influences cell mechanics, we compared cell forces in control and DP variant expressing cell pairs. Expression of DPNTP resulted in a decrease in the average intercellular tugging force and traction force per pillar compared with uninduced controls (Figure 2C). In addition, siRNA targeting endogenous DP was used to knock down DP expression (Figure 2D). DP knockdown resulted in similar effects as DPNTP when compared with scrambled siRNA controls (Figure 2E). These data suggest that uncoupling the DSM from IF reduces both cell-cell and cell-substrate forces. Notably, DP knockdown resulted in a greater decrease in the average traction force per pillar compared with DPNTP. Since DPNTP displaces endogenous DP from cell-cell contacts but does not alter DP protein levels (Figure 2A), these data raise the possibility that non-junctional DP impacts cell-substrate forces, perhaps indirectly through its ability to interact with other proteins including kinases (Albrecht *et al.*, 2015). In contrast to DPNTP, expression of S2849G DP resulted in a significant increase in cell forces when compared with controls (Figure 2C), suggesting increased DP interaction with IF enhances cell forces. Notably, expression of Wt DP alone led to a significant increase in the average traction force per pillar (Figure 2C), though to a significantly lesser extent than S2849G DP. We also observed a measurable, albeit not statistically significant, increase in the average intercellular tugging force upon expression of Wt DP (Figure 2C). These data suggest that enhancing the interaction between DSMs and IF results in an increase in cell forces. Furthermore, they suggest that the cell mechanical network is not saturated under normal conditions, and potentially there is room within the system to modulate mechanical properties through increasing or decreasing the levels of Wt protein.

Alterations in intercellular forces do not generate corresponding changes in AJ tension as detected by the α-catenin α18 epitope

Intercellular forces are transmitted cooperatively through the collective cell-cell adhesive organelles including DSMs and AJs (Bazellieres *et al.*, 2015). To determine if the changes in intercellular tugging forces observed downstream of DSM/IF modulation affected force within AJs, we employed an antibody (α18) specific for the open conformation of α-catenin, the molecular link between AJs and the actin cytoskeleton (Figure 1A), which has been previously

used to assess AJ tension (Yonemura *et al.*, 2010). Uncoupling the DSM/IF linkage by DPNTP expression led to an increase in α18 staining, while there were no notable changes in total α-catenin (Supplemental Figure 2A). This resulted in an increased ratio of α18 to total α-catenin (Supplemental Figure 2, B and C). One interpretation of these data is that AJs are under more tension upon DPNTP expression, which would be consistent with the previous observation that loss of DP increased markers of tension within AJs (Sumigray *et al.*, 2014). However, a recent study demonstrated that AJ protein clustering can induce α-catenin to enter an activated/open conformation, exposing the α18 epitope, even in the absence of force (Biswas *et al.*, 2016). Therefore, it is plausible that the increase in α18 staining observed upon expression of DPNTP, rather than being the result of increased force on α-catenin, could be the result of AJ clustering. To address this possibility, we analyzed the distribution of α-catenin using object segmentation analysis. DPNTP expression resulted in an increased number of smaller α-catenin stained clusters with increased fluorescence intensity (Supplemental Figure 2, D and E). Considering the decreased cell-cell forces measured with MA when DPNTP is expressed, our data are consistent with the possibility that DPNTP expression exposes the α18 epitope in α-catenin through a protein clustering-mediated conformational change, rather than an increase in AJ tension.

In addition, expression of Wt DP or S2849G DP had no effect on the ratio of α18 to total α-catenin (Supplemental Figure 2C), indicating that the S2849G DP-mediated effects on average intercellular tugging force are not likely facilitated through increased forces, or clustering, within AJs. It is also plausible that α-catenin already exists in a conformation that exceeds the unfolding threshold, precluding detection of additional tension downstream of DP modulation. Together, the data above suggest that the observed effects on intercellular tugging forces observed downstream of DSM/IF modulation cannot be attributed solely to alterations in actin-based AJ forces.

The DSM/IF linkage regulates cell stiffness

To complement the results obtained using the MA and to extend them to groups of cells larger than pairs, AFM cell stiffness measurements were performed on single cells, cell pairs, and cell sheets. AFM load-displacement measurements were performed by loading cells at their centroids (Figure 3, A and B). Whole cell stiffness was computed from the acquired load-deflection curves (Figure 3B). Comparisons of control and DP variant-expressing cells did not reveal stiffness changes in single cell measurements (Figure 3C). In cell pairs, the cell stiffness increased significantly upon expression of both Wt DP and S2849G DP (Figure 3C). However, expression of DPNTP and DP knockdown resulted in a significant decrease in the stiffness of cell pairs (Figure 3C). These results indicate that the DP-mediated alterations in cell forces observed using the MA are associated with corresponding changes in overall cell stiffness and are consistent with previous observations relating adherent and intercellular forces with overall levels of tension within the cytoskeleton (Ramms *et al.*, 2013; Seltmann *et al.*, 2013).

In order to assess the role of the DSM/IF network during the later stages of monolayer sheet formation, AFM was used to measure the effects of DP modulation on semiconfluent cell sheets 2 days after seeding. For all controls, cell stiffness increased as a function of confluence (Figure 3, C and D), suggesting increased cell-cell adhesion promotes mechanical stiffening. In addition,

uncoupling the DSM/IF linkage using DPNTP or DP siRNA in sheets of cells led to a significant decrease in cell stiffness compared with controls (Figure 3, D and E). In contrast, expression of S2849G DP led to a marked increase in cell stiffness in semiconfluent cell sheets (Figure 3D), while Wt DP had no effect.

It has been previously demonstrated that expression of S2849G DP in A431 cells promotes a calcium-independent, strongly adhesive state (Hobbs and Green, 2012), whereby cell sheets expressing this mutant have enhanced resistance to shear stress-induced fragmentation compared to Wt DP. Since both Wt DP and S2849G DP increase cell forces and cell stiffness, we assessed their contributions to cell stiffness in 6-day confluent sheets, where differences in shear fragmentation were previously reported (Hobbs and Green, 2012). AFM measurements showed that Wt DP and S2849G DP expression both led to significant increases in cell stiffness in 6-day confluent cell sheets, with S2849G DP inducing a significantly larger increase (Figure 3F). These data are in agreement with the MA and AFM results on cell pairs and subconfluent sheets as well as with the fragmentation data showing that enhanced IF binding properties of S2849G DP are associated with a more physically resistive state.

AFM can be used to assess the overall stiffness of an entire cell as well as to probe mechanical alterations at a subcellular level. Therefore, AFM was used to examine the mechanical properties of cytoskeletal bundles near cell-cell adhesive interfaces for cell pairs in which the DSM/IF linkage was modulated (Supplemental Figure 3A, arrows). Super-resolution imaging of these bundles demonstrate their attachment to sites of cell-cell adhesion at an orthogonal angle, an orientation normally observed for IF and not actin or microtubules (Supplemental Figure 3B). An AFM tip was used to deflect individual cytoskeletal bundles near cell-cell junctions up to a load of 0.5 nN. The maximum deflection of the tip was then used to characterize stiffness. Expression of S2849G DP and Wt DP led to a significant reduction in the measured deflections (Supplemental Figure 3C), indicating elevated stiffness of the cytoskeletal bundles. The elevation could result from an increased amount of ectopic DP expression at sites of cell-cell contact providing an increased number of IF binding sites and thus enhancing the ability of IF to resist AFM tip deflection. On the other hand, there were no differences detected upon expression of DPNTP (Supplemental Figure 3C). This suggests that while DPNTP led to retraction of the majority of IF from cell-cell junctions and an overall reduction in DSMs interacting with IF (Supplemental Figure 4), the few DSM/IF connections that do form have mechanical properties similar to controls, likely resulting from having similar levels of endogenous junctional DP. Note that the modest decrease in cytoskeletal bundles in S2849G DP-expressing cells could arise from increased IF bundling via the previously described retention of tightly bound DP S2849G along IF in the cytoplasm (Godsel *et al.*, 2005), where it could act as a crosslinker.

DSM/IF-mediated alterations in cell stiffness are dependent on actin

Since actomyosin contractility has been heavily implicated in the regulation of cell forces, we next asked if DSM/IF modulation affected actin-related signaling. Rho is a major regulator of actomyosin signaling (Kimura *et al.*, 1996). Therefore, we examined the distribution of Rho in semiconfluent cell sheets utilizing a fixation method (Yonemura *et al.*, 2004) that reveals increased Rho recruitment to lateral membranes upon activation (Figure 4 A-C) as well as staining cells with an antibody specific for active Rho bound to GTP (Figure 4, B and C). Treatment of cells with the Rho activator CN01 resulted in a significant cortical enrichment of

Rho immunostaining compared with DMSO controls (Figure 4B). DPNTP expression led to a decrease in the cortical enrichment of Rho, while Wt DP and S2849G had no detectable effects (Figure 4C). Additionally, expression of DPNTP led to a decrease in cortical filamentous actin (F-actin) at cell-cell interfaces and a decrease in the average intensity of myosin IIa on cortical F-actin (Figure 4, D and E), while total myosin IIa protein levels did not change (Figure 4F). In contrast, we were unable to detect changes in Rho, F-actin, or myosin IIa upon expression of S2849G DP. These data suggest that uncoupling the DSM/IF linkage interferes with the junctional distribution and/or activation of Rho as well as the distribution of the actomyosin machinery.

The observed alterations in Rho, F-actin, and myosin IIa in DPNTP expressing cells raised the possibility that the effects of DP modulation on cell stiffness in semiconfluent cell sheets involved the actin cytoskeleton. While changes were not detected in S2849 expressing cells, this did not rule out a role for actin in affecting the increased stiffness observed in these cells. Towards directly addressing a role for actin, multiple concentrations of the actin disrupting drug cytochalasin D (CytoD) were used to destabilize the actin network in semiconfluent A431 cells (Figure 5A). DSMs appeared to still be present at all dosages, as assessed by a "railroad" pattern of cytoplasmic plaque DP staining at cell-cell contacts (Figure 5B) (Chen *et al.*, 2012). Destabilization of the actin network led to a dose-dependent decrease in cell stiffness (Figure 5C). Since the highest concentration of CytoD used (2.5 μM) led to an almost complete loss of F-actin (Figure 5A), the middle (250 nM) and low (50 nM) doses were used to assess the involvement of the actin network downstream of DSM/IF modulation. When induced A431 cell lines were treated with 250 nM CytoD, Wt DP, DPNTP, and S2849G DP localized to cell-cell junctions and Wt DP and S2849G DP exhibited a "railroad" pattern (Figure 5D), suggesting maintenance of the structural integrity of DSMs. The effects of both DPNTP and S2849G DP expression on cell stiffness were abrogated by destabilizing the actin network using both the middle and low doses of CytoD (Figure 5E).

Collectively, these data demonstrate that changes in cell forces due to modulation of the DSM/IF network is strongly dependent on the actin cytoskeleton. In the case of IF uncoupling through expression of DPNTP, interference with junctional Rho may contribute to the observed changes. While we cannot rule out that changes in Rho occurred in S2849G DP expressing cells that were not detected in our assays, other pathways such as actin-bundling, cortical stiffening (e.g., ezrin, radixin and moesin), or kinase signaling linked to DP may also be involved in governing the observed alterations in cell mechanics (Tseng *et al.*, 2005; Fehon *et al.*, 2010; Albrecht *et al.*, 2015).

Our work is consistent with the following model. Under isometric tension, cells contain tensile elements and compressive elements. While, the tensile component is widely thought to comprise the actomyosin machinery (Ingber, 2008), our data support the DSM/IF network functioning as a compressive element, resisting tension generated by actomyosin. Recently, it has been suggested that keratin IF can be under compressive forces (Nolting *et al.*, 2014) and that vimentin IF act to resist forces generated by actomyosin (Jiu *et al.*, 2015). Therefore, strengthening the DSM/IF network could increase the resistive capacity of the system by carrying greater compressive forces, allowing for more robust actomyosin-generated tension and increased cell forces/stiffness, while disruption would lead to the opposite effects (Figure 5F).

There are approximately 70 genes that encode IF products, some containing alternative splice forms, with similar structural organization but different primary amino acid sequences (Herrmann *et al.*, 2009). Moreover, there are more than 10 genes encoding the core DSM components, some with multiple isoforms (Garrod and Chidgey, 2008). This provides an immense array of diversity within the composition of DSM/IF networks and potentially provides the capacity to finely tune mechanics based on tissue- and differentiation-dependent expression of these components. DSM/IF-mediated tuning of the mechanical force balance among the cytoskeletal systems is likely critical for regulating a cell's ability to respond to force stimuli and signal through mechanotransduction pathways.

Methods and Materials

Micropillar substrate fabrication and functionalization. PDMS MA substrates were fabricated by following previously published protocols with some modifications. The patterns on a photomask were first transferred onto the photoresist layer on a silicon wafer using conventional contact lithography. A silicon wafer spin coated with a uniform layer of 1.2 μm-thick photoresist S1813 was exposed to UV light in a MABA6 aligner (Karl Suss, Munich, Germany), followed by developing in the developer MF-351 solution. The patterned photoresist layer then served as the mask to pattern the silicon wafer using deep reactive ion etching (DRIE, STS LpX Pegasus). Silicon micropost arrays with a height of approximately 10 μm were obtained after carefully controlled DRIE etching. Two sequential PDMS replica-molding steps were performed to obtain PDMS micropost arrays from the silicon micropost arrays. Prior to the first replica-molding step, the silicon mold was cleaned with oxygen plasma and then coated with a surfactant self-assembled monolayer, tridecafluoro-(1,1,2,2)-tetrahydrooctyl trichlorosilane (FOTS, Gelest) to lower surface energy. More specifically, the silicon wafer was immersed in a 0.5% wt solution of FOTS in heptane at 65°C for 5 min, followed by cleaning in pure heptane solution to remove redundant surfactant and 10 min baking at 100°C to improve the strength of the release layer. To make the PDMS negative mold, a mixture of elastomer and curing agent at a 10:1 ratio was poured onto the silicon mold, placed in a vacuum for 45 min, and heated to 100°C on a hotplate for 2 h. The PDMS was then peeled off from the silicon mold, yielding the negative mold. The same surface treatment was performed to the negative mold prior to the second replica-molding step. The same PDMS solution, as used in the previous step, was coated on each PDMS negative mold with a thickness of approximately 2 mm. The coated molds were placed in a vacuum for at least 1 h to ensure that the liquid PDMS fully filled in the high-aspect-ratio holes without gas trapping. Then each PDMS mold was turned over and placed on a clean glass substrate and cured on a hotplate at 100°C for 2 h. The baking time was kept equal for all batches of samples to ensure consistent mechanical properties of the cured PDMS pillars. After immersion in isopropanol for at least 6 h, the PDMS MA were manually peeled off from the negative mold. Finally, critical-point drying (Tousimis Automegasamdri - 915B, Series C) was performed to remove the isopropanol without collapsing the pillars. The fabricated PDMS pillar arrays were characterized using scanning electron microscopy (FEI Nova 600) and 3D profilometer (ZYGO).

Surface functionalization. PDMS stamps were prepared by curing the mixture of elastomer and curing agent at 15:1 ratio in a clean petri dish and then cut into individual pieces of similar size to the MA substrate. After sequential cleaning in isopropanol and distilled water, a mixture of

fibronectin and Alex Fluor conjugated IgG antibodies, at a weight ratio of 4:1 with a total weight concentration of 50 μg/ml, was pipetted onto the tops of PDMS stamps with the face in contact with the petri dish bottom surface facing up. Excess solution was carefully removed using a kimwipe after 1 h incubation at room temperature. The stamps were blow-dried with nitrogen. The MA substrates were treated with a UV-ozone cleaner (BioForce, Ames, USA) for 7 min. Immediately after the UV-ozone treatment, the stamps were flipped over to allow their top surfaces to make contact with the top of the MA and gently pressed with a tweezer. After separating the stamps from the MA, the substrates were sterilized and rinsed by sequentially dipping the substrates into 100% isopropanol and 70% isopropanol, followed by distilled water for three times. The substrates were then incubated in 0.2% pluronics F-127 in phosphate-buffered saline for 45 min at room temperature, followed by rinsing twice in sterile PBS.

Cell culture, pharmacological treatments, and RNAi. A431 cells were maintained in DMEM (Corning, Corning, NY) supplemented with 10% fetal bovine serum (Sigma-Aldrich, St. Louis, MO) and 1% penicillin-streptomycin (Corning) (growth medium) at 37°C with 5% CO_2. Stable A431 cell lines were generated by transfecting parental cells with pTet-On (Clontech, Mountain View, CA), followed by selection with 400 μg/ml G418 (Corning), and subsequently transfecting with pTRE (Clontech) plasmids expressing DPNTP-GFP, DP-S2849G-GFP, or wild-type DP-GFP (Huen *et al.*, 2002; Godsel *et al.*, 2005). For induction, cells were cultured with 4 μg/mL doxycycline (Sigma-Aldrich) in growth medium for 18 h. Subsequently, both non-induced and induced cells were plated at low density onto MA and cultured overnight. Pharmacological treatments modulating cell contractility included 3 μM blebbistatin (Sigma-Aldrich) for 2 h and 1 unit/mL Rho Activator I (CN01; Cytoskeleton, Inc., Denver, CO) for 30 min. Parental A431 cells were transfected with either siGENOME Non-Targeting siRNA Pool #2 or siGENOME SMARTpool siRNA D-019800-17 DSP (Dharmacon, Lafayette, CO) using DharmaFECT (GE Healthcare, Pittsburgh, PA), according to the manufacturer's instructions.

Immunofluorescence, image acquisition, and image quantification. A431 cells cultured on either glass coverslips (VWR, Radnor, PA) or MA were rinsed with phosphate-buffered saline, fixed in 4% paraformaldehyde for 10 min, with or without subsequent fixation using anhydrous methanol for 3 min, and processed for immunofluorescence. Trichloroacetic acid (Sigma-Aldrich) fixation for RhoA antibody staining was performed as previously described (Yonemura *et al.*, 2004). Primary antibodies included: KSB 17.2 (Sigma-Aldrich), 1407 (Aves Labs, Inc., Tigard, OR), HECD-1 (a gift from Drs. Masatoshi Takeichi and Osahiko Abe, RIKEN Center for Developmental Biology, Kobe, Japan), 1G5 (a gift from Dr. Margaret Wheelock), α18 (a gift from Dr. Akira Nagafuchi, Nara Medical University, Japan), DM1A (Sigma-Aldrich), Myosin IIa Antibody (Cell Signaling Technology, Danvers, MA), RhoA Antibody (26C4) (Santa Cruz Biotechnology, Dallas, TX), and Anti-Active RhoA Mouse Monoclonal Antibody (RhoGTP, NewEast Biosciences, King of Prussia, PA). Secondary antibodies included: Alexa Fluor® 488, 568, and 647 conjugated anti-mouse, -rabbit, or -chicken IgG (Life Technologies, Grand Island, NY). Alexa Fluor® 568 phalloidin (Life Technologies) was used to visualize filamentous actin.

Apotome images were acquired using an epifluorescence microscope system (AxioVision Z1; Carl Zeiss, Thornwood, NY) fitted with an Apotome slide module, AxioCam MRm digital camera, and a 40× 0.5 EC Plan-Neofluar or 100× 1.4 NA oil Plan-Apochromat objective (Carl Zeiss). Super-resolution images were acquired using a Nikon TiE N-SIM system with a 100×

objective lens (NA 1.40) (Nikon, Tokyo, Japan) and an iXon X3 897 camera (Andor Technology, Belfast, United Kingdom). SIM images were reconstructed using NIS Elements version 4.20.01 software (Build 982, Nikon). Confocal images were acquired using a Nikon A1R Confocal Laser microscope equipped with GaAsP detectors, a 60x Plan-Apochromat objective lambda with an NA of 1.4, and run by NIS Elements software (Nikon).

To quantify the number of IF bundles attached at sites of cell-cell contact, immunofluorescence was used to visualize both keratin bundles (KSB 17.2) and cell junctions (PG, 1407). IF bundles entering perpendicular to the cell junctions were quantified with ImageJ software (NIH). The number of IF bundles was divided by border length (in pixels) and then averaged for each condition. The average fluorescence intensity of total α-catenin (1G5), α18, the ratio of α18 to total α-catenin, the cortical to noncortical ratio of either total Rho or RhoGTP staining at cell-cell junctions, as well as myosin IIa staining on cortical actin (identified with phalloidin staining) were quantified using MetaMorph version 7.8.0.0 software (Molecular Devices LLC., Sunnyvale, CA). A linescan analysis (5 pixels wide) of phalloidin (F-actin) staining at cell-cell junctions was performed using MetaMorph software. Object segmentation analysis of α-catenin staining was performed using the Integrated Morphometry Analysis function in MetaMorph to calculate the average object number, size, and intensity per cell-cell border. All image analysis experiments were performed for at least 3 independent experiments.

AFM imaging and force measurements. Control and induced A431 cells were cultured in growth medium at 37°C and 5% CO_2 for either 2 or 6 days before experiments. For siRNA knock down, experiments were carried out 3 days after DharmaFECT transfection with siRNA (40 nM). For the actin depolymerization experiments, cells were incubated with CytoD (2.5 μM, 250 nM, or 50 nM) for 1 h at 37°C, and DMSO was used as a control. AFM imaging and force measurements of live cells were carried out in cell growth medium at 37°C using the Peakforce Tapping mode on a Catalyst AFM (Bruker Nano, Inc., Santa Barbara, CA). A silicon nitride cantilever with a tip radius of approximately 20 nm and a nominal spring constant of 0.3 N/m (Bruker Nano, Inc.), calibrated using the thermal tune method (Lévy and Maaloum, 2002), was used for force measurements. Both trace and re-trace curves were analyzed. The approach speed was set at 0.5 μm/s to reduce the effects of cell viscosity. Collected force curves were processed with Matlab routine to convert them into stiffness values using the Sneddon model (Cappella and Dietler, 1999). The tip half opening angle was 17.5° and the Poisson ratio was 0.5.

Acknowledgements
This work is supported by NIH grants from NIAMS (AR042836 and AR043380) and NCI (CA122151). J. Broussard was supported by a Training Grant: Post Graduate Program in Cutaneous Biology (T32 AR060710). The authors acknowledge support from the McCormick School of Engineering through a catalyst award and the Chicago Biomedical Consortium with support from the Searle Funds at The Chicago Community Trust. Imaging work was performed at the Northwestern University Center for Advanced Microscopy generously supported by NCI CCSG P30 CA060553 awarded to the Robert H Lurie Comprehensive Cancer Center. Structured illumination microscopy was performed on a Nikon N-SIM system, purchased through the support of NIH 1S10OD016342-01.

References

Aguilar-Cuenca, R., Juanes-García, A., and Vicente-Manzanares, M. (2014). Myosin II in mechanotransduction: master and commander of cell migration, morphogenesis, and cancer. Cell. Mol. Life Sci. *71*, 479-492.

Albrecht, L.V., Zhang, L., Shabanowitz, J., Purevjav, E., Towbin, J.A., Hunt, D.F., and Green, K.J. (2015). GSK3- and PRMT-1-dependent modifications of desmoplakin control desmoplakin-cytoskeleton dynamics. J Cell Biol *208*, 597-612.

Bazellieres, E., Conte, V., Elosegui-Artola, A., Serra-Picamal, X., Bintanel-Morcillo, M., Roca-Cusachs, P., Munoz, J.J., Sales-Pardo, M., Guimera, R., and Trepat, X. (2015). Control of cell-cell forces and collective cell dynamics by the intercellular adhesome. Nat Cell Biol *17*, 409-420.

Benham-Pyle, B.W., Pruitt, B.L., and Nelson, W.J. (2015). Cell adhesion. Mechanical strain induces E-cadherin-dependent Yap1 and beta-catenin activation to drive cell cycle entry. Science *348*, 1024-1027.

Biswas, K.H., Hartman, K.L., Zaidel-Bar, R., and Groves, J.T. (2016). Sustained alpha-catenin Activation at E-cadherin Junctions in the Absence of Mechanical Force. Biophys J *111*, 1044-1052.

Borghi, N., Sorokina, M., Shcherbakova, O.G., Weis, W.I., Pruitt, B.L., Nelson, W.J., and Dunn, A.R. (2012). E-cadherin is under constitutive actomyosin-generated tension that is increased at cell–cell contacts upon externally applied stretch. Proceedings of the National Academy of Sciences *109*, 12568-12573.

Bornslaeger, E.A., Corcoran, C.M., Stappenbeck, T.S., and Green, K.J. (1996). Breaking the connection: displacement of the desmosomal plaque protein desmoplakin from cell-cell interfaces disrupts anchorage of intermediate filament bundles and alters intercellular junction assembly. J Cell Biol *134*, 985-1001.

Broussard, J.A., Getsios, S., and Green, K.J. (2015). Desmosome regulation and signaling in disease. Cell Tissue Res *360*, 501-512.

Brunner, C., Ehrlicher, A., Kohlstrunk, B., Knebel, D., Käs, J., and Goegler, M. (2006). Cell migration through small gaps. Eur Biophys J *35*, 713-719.

Cappella, B., and Dietler, G. (1999). Force-distance curves by atomic force microscopy. Surface Science Reports *34*, 1-104.

Chen, J., Nekrasova, O.E., Patel, D.M., Klessner, J.L., Godsel, L.M., Koetsier, J.L., Amargo, E.V., Desai, B.V., and Green, K.J. (2012). The C-terminal unique region of desmoglein 2 inhibits its internalization via tail-tail interactions. J Cell Biol *199*, 699-711.

Cohen, D.M., Yang, M.T., and Chen, C.S. (2013). Measuring cell-cell tugging forces using bowtie-patterned mPADs (microarray post detectors). Methods Mol Biol *1066*, 157-168.

de Rooij, J. (2014). Cadherin adhesion controlled by cortical actin dynamics. Nat Cell Biol *16*, 508-510.

DuFort, C.C., Paszek, M.J., and Weaver, V.M. (2011). Balancing forces: architectural control of mechanotransduction. Nat Rev Mol Cell Biol *12*, 308-319.

Eyckmans, J., Boudou, T., Yu, X., and Chen, C.S. (2011). A hitchhiker's guide to mechanobiology. Dev Cell *21*, 35-47.

Fehon, R.G., McClatchey, A.I., and Bretscher, A. (2010). Organizing the cell cortex: the role of ERM proteins. Nat Rev Mol Cell Biol *11*, 276-287.

Galbraith, C.G., and Sheetz, M.P. (1999). Keratocytes pull with similar forces on their dorsal and ventral surfaces. J Cell Biol *147*, 1313-1324.

Garrod, D., and Chidgey, M. (2008). Desmosome structure, composition and function. Biochimica et Biophysica Acta (BBA) - Biomembranes *1778*, 572-587.

Godsel, L.M., Hsieh, S.N., Amargo, E.V., Bass, A.E., Pascoe-McGillicuddy, L.T., Huen, A.C., Thorne, M.E., Gaudry, C.A., Park, J.K., Myung, K., Goldman, R.D., Chew, T.L., and Green, K.J. (2005). Desmoplakin

assembly dynamics in four dimensions: multiple phases differentially regulated by intermediate filaments and actin. J Cell Biol *171*, 1045-1059.
Grashoff, C., Hoffman, B.D., Brenner, M.D., Zhou, R., Parsons, M., Yang, M.T., McLean, M.A., Sligar, S.G., Chen, C.S., Ha, T., and Schwartz, M.A. (2010). Measuring mechanical tension across vinculin reveals regulation of focal adhesion dynamics. Nature *466*, 263-266.
Green, A., Green, H., Rehnberg, M., Svensson, A., Gunnarsson, C., and Jonasson, J. (2015). Assessment of HaloPlex amplification for sequence capture and massively parallel sequencing of arrhythmogenic right ventricular cardiomyopathy-associated genes. J Mol Diagn *17*, 31-42.
Harris, A.R., Daeden, A., and Charras, G.T. (2014). Formation of adherens junctions leads to the emergence of a tissue-level tension in epithelial monolayers. J Cell Sci *127*, 2507-2517.
Herrmann, H., Strelkov, S.V., Burkhard, P., and Aebi, U. (2009). Intermediate filaments: primary determinants of cell architecture and plasticity. J Clin Invest *119*, 1772-1783.
Hobbs, R.P., and Green, K.J. (2012). Desmoplakin regulates desmosome hyperadhesion. J Invest Dermatol *132*, 482-485.
Huen, A.C., Park, J.K., Godsel, L.M., Chen, X., Bannon, L.J., Amargo, E.V., Hudson, T.Y., Mongiu, A.K., Leigh, I.M., Kelsell, D.P., Gumbiner, B.M., and Green, K.J. (2002). Intermediate filament-membrane attachments function synergistically with actin-dependent contacts to regulate intercellular adhesive strength. J Cell Biol *159*, 1005-1017.
Ingber, D.E. (2008). Tensegrity-based mechanosensing from macro to micro. Progress in biophysics and molecular biology *97*, 163-179.
Jaalouk, D.E., and Lammerding, J. (2009). Mechanotransduction gone awry. Nat Rev Mol Cell Biol *10*, 63-73.
Jiu, Y., Lehtimaki, J., Tojkander, S., Cheng, F., Jaalinoja, H., Liu, X., Varjosalo, M., Eriksson, J.E., and Lappalainen, P. (2015). Bidirectional Interplay between Vimentin Intermediate Filaments and Contractile Actin Stress Fibers. Cell reports *11*, 1511-1518.
Kimura, K., Ito, M., Amano, M., Chihara, K., Fukata, Y., Nakafuku, M., Yamamori, B., Feng, J., Nakano, T., Okawa, K., Iwamatsu, A., and Kaibuchi, K. (1996). Regulation of myosin phosphatase by Rho and Rho-associated kinase (Rho-kinase). Science *273*, 245-248.
Kress, H., Stelzer, E.H., Holzer, D., Buss, F., Griffiths, G., and Rohrbach, A. (2007). Filopodia act as phagocytic tentacles and pull with discrete steps and a load-dependent velocity. Proc Natl Acad Sci U S A *104*, 11633-11638.
Legant, W.R., Choi, C.K., Miller, J.S., Shao, L., Gao, L., Betzig, E., and Chen, C.S. (2013). Multidimensional traction force microscopy reveals out-of-plane rotational moments about focal adhesions. Proc Natl Acad Sci U S A *110*, 881-886.
Levental, K.R., Yu, H., Kass, L., Lakins, J.N., Egeblad, M., Erler, J.T., Fong, S.F., Csiszar, K., Giaccia, A., Weninger, W., Yamauchi, M., Gasser, D.L., and Weaver, V.M. (2009). Matrix crosslinking forces tumor progression by enhancing integrin signaling. Cell *139*, 891-906.
Lévy, R., and Maaloum, M. (2002). Measuring the spring constant of atomic force microscope cantilevers: thermal fluctuations and other methods. Nanotechnology *13*, 33.
Liu, Z., Tan, J.L., Cohen, D.M., Yang, M.T., Sniadecki, N.J., Ruiz, S.A., Nelson, C.M., and Chen, C.S. (2010). Mechanical tugging force regulates the size of cell-cell junctions. Proc Natl Acad Sci U S A *107*, 9944-9949.
Maruthamuthu, V., Sabass, B., Schwarz, U.S., and Gardel, M.L. (2011). Cell-ECM traction force modulates endogenous tension at cell–cell contacts. Proceedings of the National Academy of Sciences *108*, 4708-4713.
Meng, J.J., Bornslaeger, E.A., Green, K.J., Steinert, P.M., and Ip, W. (1997). Two-hybrid analysis reveals fundamental differences in direct interactions between desmoplakin and cell type-specific intermediate filaments. J Biol Chem *272*, 21495-21503.

Mertz, A.F., Che, Y., Banerjee, S., Goldstein, J.M., Rosowski, K.A., Revilla, S.F., Niessen, C.M., Marchetti, M.C., Dufresne, E.R., and Horsley, V. (2013). Cadherin-based intercellular adhesions organize epithelial cell-matrix traction forces. Proc Natl Acad Sci U S A *110*, 842-847.
Nolting, J.F., Mobius, W., and Koster, S. (2014). Mechanics of individual keratin bundles in living cells. Biophys J *107*, 2693-2699.
Prass, M., Jacobson, K., Mogilner, A., and Radmacher, M. (2006). Direct measurement of the lamellipodial protrusive force in a migrating cell. J Cell Biol *174*, 767-772.
Ramms, L., Fabris, G., Windoffer, R., Schwarz, N., Springer, R., Zhou, C., Lazar, J., Stiefel, S., Hersch, N., Schnakenberg, U., Magin, T.M., Leube, R.E., Merkel, R., and Hoffmann, B. (2013). Keratins as the main component for the mechanical integrity of keratinocytes. Proc Natl Acad Sci U S A *110*, 18513-18518.
Schoen, I., Hu, W., Klotzsch, E., and Vogel, V. (2010). Probing cellular traction forces by micropillar arrays: contribution of substrate warping to pillar deflection. Nano Lett *10*, 1823-1830.
Seltmann, K., Fritsch, A.W., Kas, J.A., and Magin, T.M. (2013). Keratins significantly contribute to cell stiffness and impact invasive behavior. Proc Natl Acad Sci U S A *110*, 18507-18512.
Simpson, C.L., Patel, D.M., and Green, K.J. (2011). Deconstructing the skin: cytoarchitectural determinants of epidermal morphogenesis. Nat Rev Mol Cell Biol *12*, 565-580.
Sumigray, K., Zhou, K., and Lechler, T. (2014). Cell-cell adhesions and cell contractility are upregulated upon desmosome disruption. PLoS One *9*, e101824.
Tan, J.L., Tien, J., Pirone, D.M., Gray, D.S., Bhadriraju, K., and Chen, C.S. (2003). Cells lying on a bed of microneedles: an approach to isolate mechanical force. Proc Natl Acad Sci U S A *100*, 1484-1489.
Tseng, Y., Kole, T.P., Lee, J.S., Fedorov, E., Almo, S.C., Schafer, B.W., and Wirtz, D. (2005). How actin crosslinking and bundling proteins cooperate to generate an enhanced cell mechanical response. Biochem Biophys Res Commun *334*, 183-192.
Yang, M.T., Fu, J., Wang, Y.K., Desai, R.A., and Chen, C.S. (2011). Assaying stem cell mechanobiology on microfabricated elastomeric substrates with geometrically modulated rigidity. Nat Protoc *6*, 187-213.
Yonemura, S., Hirao-Minakuchi, K., and Nishimura, Y. (2004). Rho localization in cells and tissues. Exp Cell Res *295*, 300-314.
Yonemura, S., Wada, Y., Watanabe, T., Nagafuchi, A., and Shibata, M. (2010). alpha-Catenin as a tension transducer that induces adherens junction development. Nat Cell Biol *12*, 533-542.

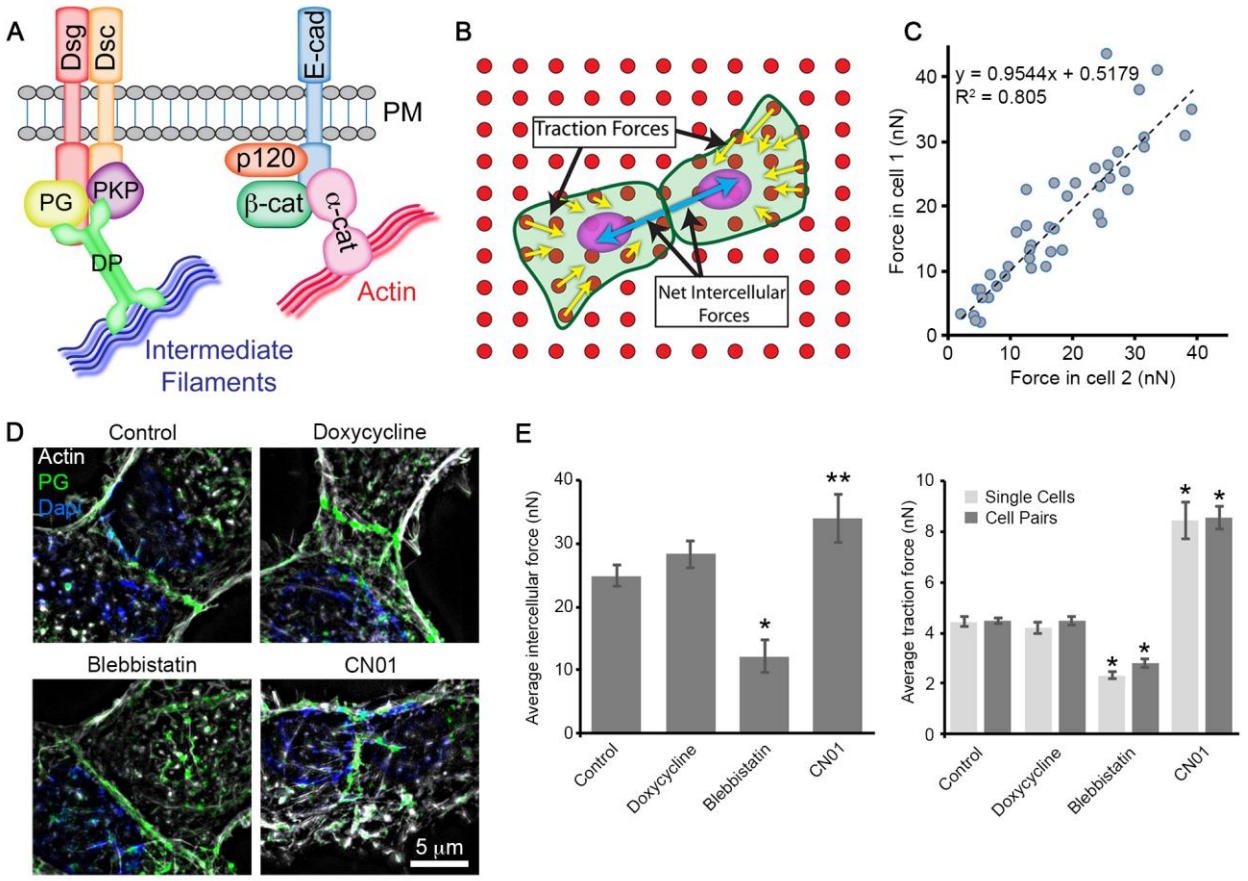

Figure 1. Quantification of cell-substrate and cell-cell adhesion using MA. (A) Schematic representation of the major protein constituents of DSMs (left) and AJs (right): PM, plasma membrane; DP, desmoplakin; Dsg, desmoglein; Dsc, desmocollin; PKP, plakophilin; PG, plakoglobin; E-cad, E-cadherin; p120, p120 catenin; β-cat, β-catenin; and α-cat, α-catenin. (B) Schematic representation of forces measured with MA. Cells (green) displace pillar tips (red) through traction forces (yellow arrows). Within cell pairs, the sum of the traction forces can be used to quantify net intercellular forces (blue arrows), which are equal and opposite in magnitude. (C) Force balance between cell pairs. The dashed line represents a linear regression and the corresponding equation is shown. The theoretical condition where the force in cell 1 equals the force in cell 2 would have a slope m=1. (D) Super-resolution micrographs of cells treated with the indicated compounds are shown with actin in white, plakoglobin (PG) in green to indicate the cell-cell junction, and Dapi in blue to show nuclei. (E) The average intercellular force and the average traction force per pillar are shown for cells treated with the indicated compounds. Error bars represent the standard error of the mean for 7-28 cells from 3 independent experiments. *p<0.001, **p=0.02.

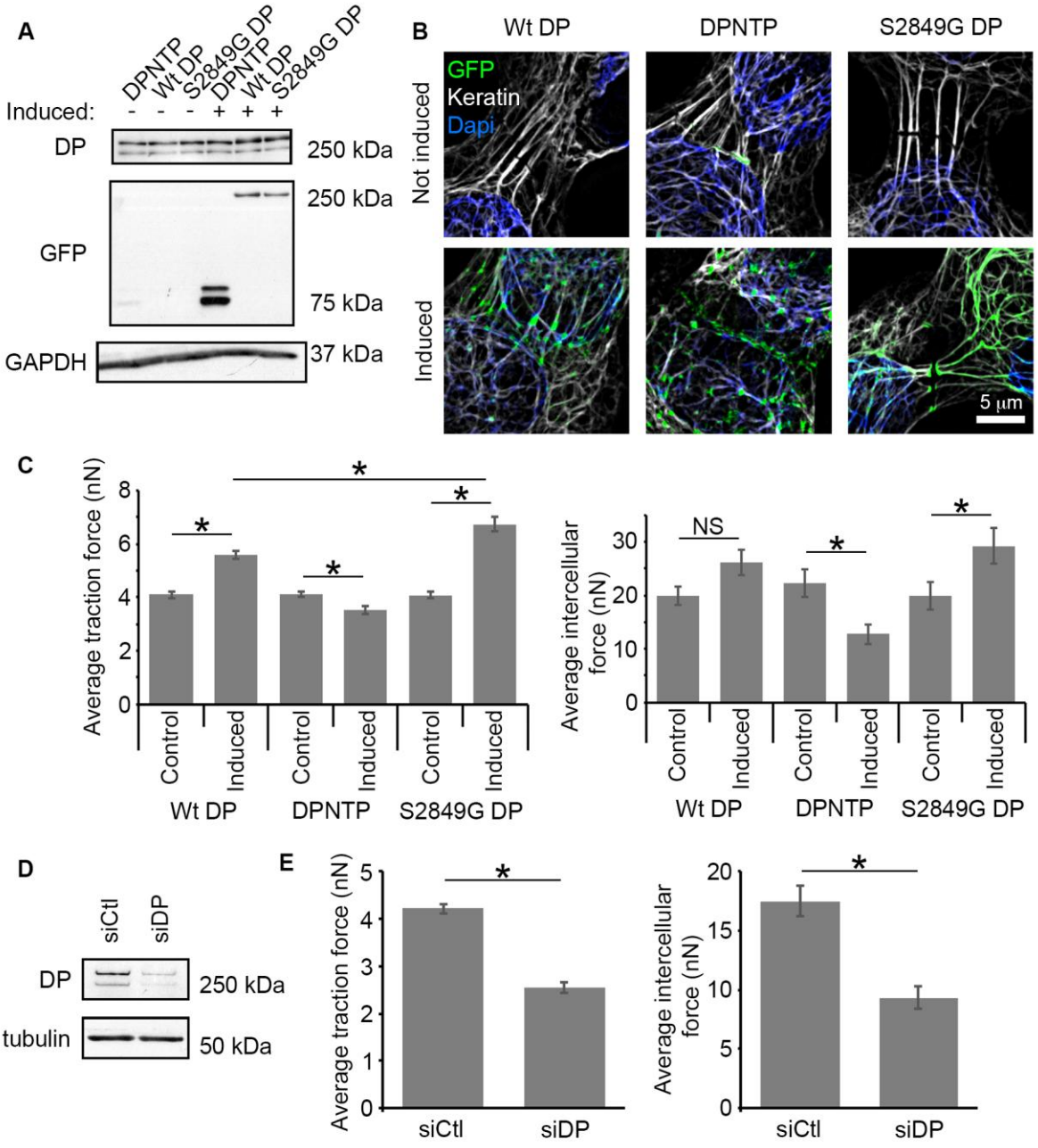

Figure 2. Modulating the DSM/IF connection leads to alterations in cell traction and tugging forces. (A) Western blot showing the expression of endogenous DP and doxycycline-induced expression of GFP-tagged DP variants. GAPDH is shown as a loading control. (B) Super-resolution micrographs of control cells (not induced) and cells induced to express GFP-tagged DP variants are shown. The GFP-tagged DP variants are shown in green, keratin IF are shown in white, and Dapi indicates nuclei in blue. (C) The average traction force per pillar and the average intercellular force are shown for control cells and cells induced to express the indicated DP variants. Error bars represent the standard error of the mean from at least 18 cells from 3 independent experiments. *$p<0.05$. (D) Representative western blot indicating knock down of endogenous DP in cells treated with either non-targeting siRNA (siCtl) or siRNA targeting DP

(siDP). Tubulin is shown as a loading control. (E) The average traction force per pillar and the average intercellular force are shown for cells treated with either non-targeting siRNA (siCtl) or siRNA targeting DP (siDP). Error bars represent the standard error of the mean from at least 30 cells from 3 independent experiments. *$p<0.0001$.

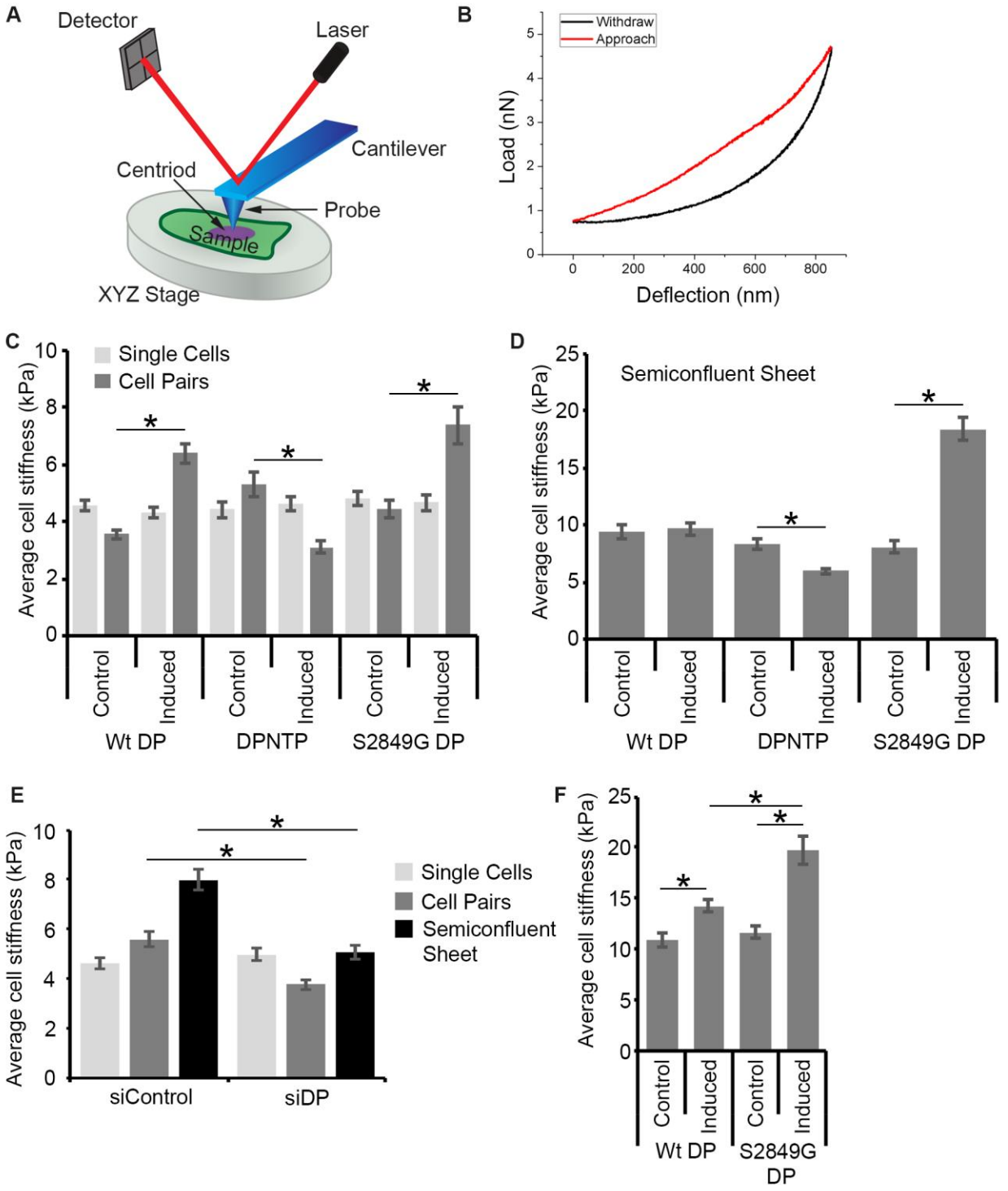

Figure 3. The DSM/IF network regulates cell stiffness. (A) Schematic diagram of an atomic force microscope. A cantilever is used to probe the physical properties of a cell. The displacement of the cantilever is determined by the movement of a laser across a detector. (B) A Load vs. Deflection function for both the approach and withdrawal of the AFM tip is shown. (C) Average cell stiffness measurements on single cells and cell pairs for cells expressing the

indicated DP variants are shown (control and induced conditions). All force displacement curves were taken by AFM on the cell centroid and were converted to stiffness using the Hertz model. Error bars represent the standard error of the mean from at least 45 cells from 3 independent experiments. *$p<0.0001$. (D) Average cell stiffness measurements of individual cells within semiconfluent (80%) cell sheets for cells expressing the indicated DP variants are shown (control and induced conditions). Error bars represent the standard error of the mean from at least 91 cells from 3 independent experiments. *$p<0.0001$. (E) Average cell stiffness measurements on single cells, cell pairs, and cell sheets for DP knockdown (siDP) and non-targeting siRNA control (siCtl) conditions are shown. Error bars represent the standard error of the mean from at least 55 cells from 3 independent experiments. *$p<0.0001$. (F) Average cell stiffness measurements of calcium-insensitive, confluent cell sheets for cells expressing the indicated DP variants are shown. Error bars represent the standard error of the mean from at least 58 cells from 3 independent experiments. *$p\leq0.0002$.

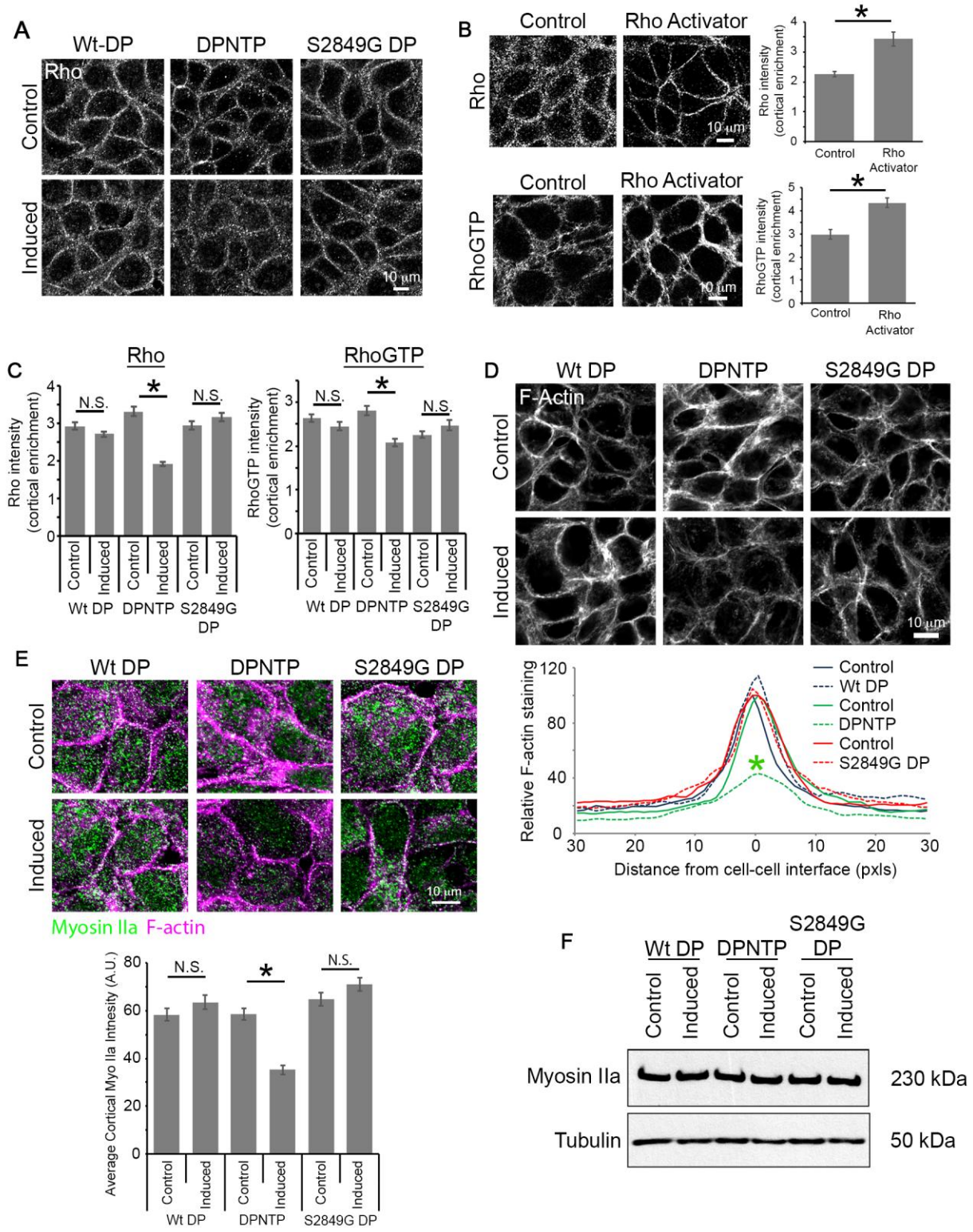

Figure 4. Disrupting the DSM/IF connection affects Rho, F-actin, and myosin IIa distribution. (A) Confocal micrographs of Rho immunostaining in control cells (not induced) and cells induced to express GFP-tagged DP variants and fixed with 10% trichloroacetic acid (TCA) are

shown. (B) Confocal micrographs of cells treated with the Rho activator CN01 and immunostained with a total Rho (fixed with 10% TCA) or a RhoGTP (fixed with 4% PFA) antibody are shown. Control cells were treated with DMSO. Right, quantification of the cortical enrichment (cortical to non-cortical ratio) of the indicated immunostaining is shown. Error bars represent the standard error of the mean from at least 30 cells from 3 independent experiments. *$p<0.0001$. (C) Quantification of the cortical enrichment (cortical to non-cortical ratio) of total Rho and RhoGTP for control cells (not induced) and cells induced to express GFP-tagged DP variants are shown. Error bars represent the standard error of the mean from at least 50 cells from 3 independent experiments. *$p<0.0001$. (D) Confocal micrographs of phalloidin staining (F-actin) in control cells (uninduced) and cells induced to express GFP-tagged DP variants are shown. Right, linescan analysis of the intensity of phalloidin staining as a function of distance from cell-cell interfaces for uninduced cells (Control) and cells induced to express the indicated GFP-tagged DP variants is shown. Green asterisk denotes significant difference upon expression of DPNTP; *$p=0.0005$ from 20 cells from 3 independent experiments. (E) Apotome micrographs of control cells (not induced) and cells induced to express GFP-tagged DP variants that were stained with phalloidin (F-actin) and myosin IIa are shown. Below, quantification of the average intensity of myosin IIa on cortical F-actin in control cells (uninduced) and cells induced to express GFP-tagged DP variants is shown. Error bars represent the standard error of the mean from at least 55 cells from 3 independent experiments. *$p<0.0001$. (F) Representative western blot indicating the level of myosin IIa in the indicated cells. Tubulin is shown as a loading control.

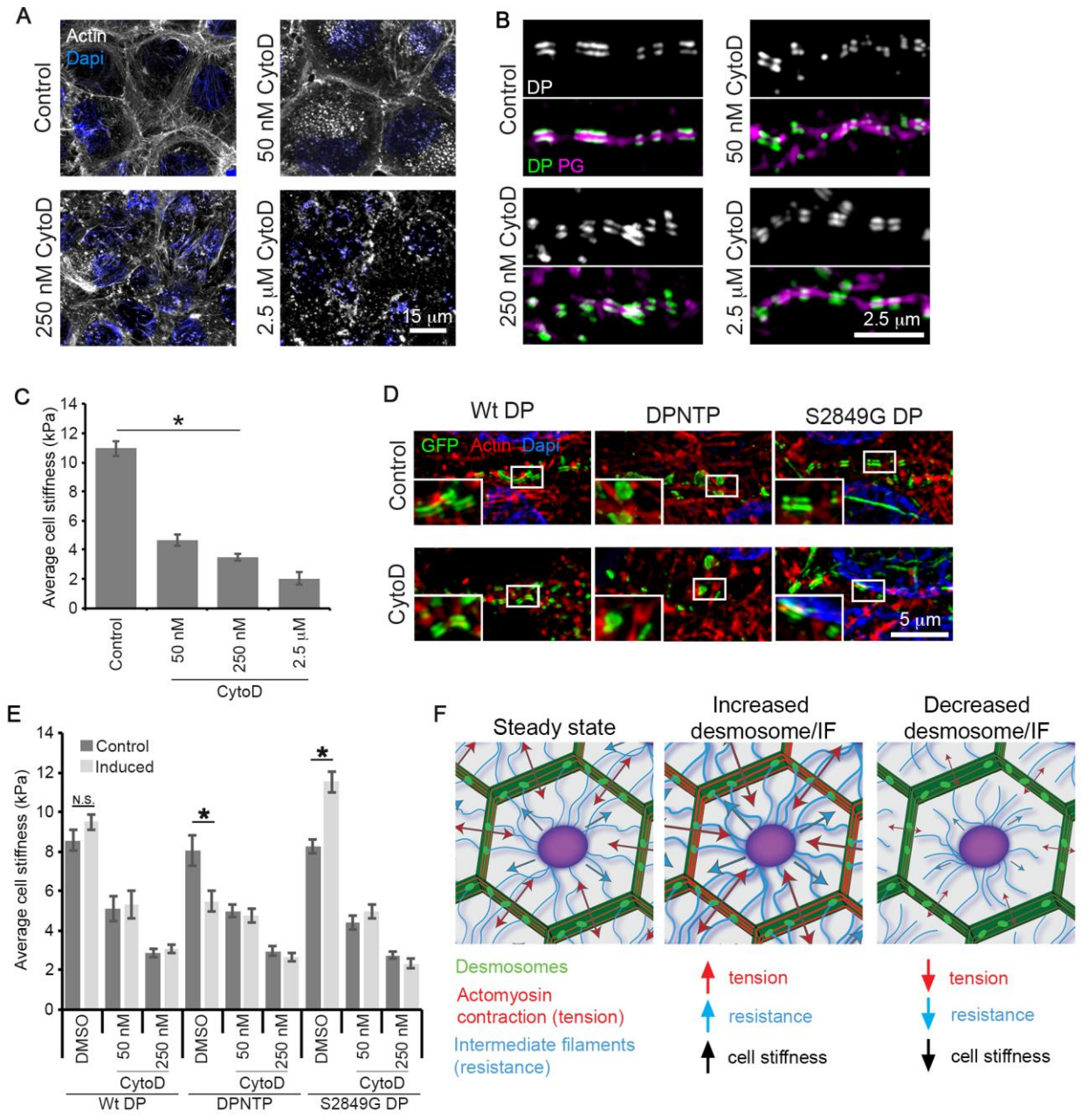

Figure 5. The DSM/IF-mediated effects on cell stiffness are dependent on the actin cytoskeleton. (A) Apotome micrographs of cells treated with the indicated concentrations of the actin depolymerization agent cytochalasins D (CytoD) are shown with actin filaments (phalloidin staining) in white and Dapi in blue to show nuclei. DMSO was used as the control. (B) Super-resolution micrographs of cells treated with the indicated concentrations of CytoD are shown with staining of desmoplakin (DP) in white (above) and in green (below) overlayed with plakoglobin (PG) in magenta at representative cell-cell junctions. DMSO was used as the control. (C) Average cell stiffness measurements of individual cells within semiconfluent (80%) cell sheets for cells treated with the indicated concentrations of CytoD are shown. DMSO was used as a control. Error bars represent the standard error of the mean from at least 99 cells from 3

independent experiments. *p<0.0001. (D) Super-resolution micrographs of induced A431 cells expressing GFP-tagged DP variants and treated with 250 nM CytoD are shown. The GFP-tagged DP variants are shown in green, actin filaments (phalloidin staining) are shown in white, and Dapi indicates nuclei in blue. (E) Average cell stiffness measurements of individual induced or uninduced (control) A431 cells within semiconfluent (80%) cell sheets and treated with the indicated concentrations of CytoD or DMSO as a control are shown. Error bars represent the standard error of the mean from at least 30 cells from 3 independent experiments. *p<0.01. (F) Model: the desmosome/IF linkage regulates the balance of cell forces. Cells exist in a "prestressed" state, which allows the system to respond rapidly to mechanical stimuli. There are tensile elements (red) and there are compressive elements (blue) that resist this tension. The tensile component is widely thought to be comprised of the actomyosin machinery. Our data support a model in which the DSM/IF network may be functioning to resist the tension generated by actomyosin contractility. In this model, strengthening the DSM/IF connection leads to an increased resistive capacity of the system, allowing for more robust actomyosin-generated tension and increased cell forces/stiffness. However, uncoupling the DSM/IF network would decrease the resistive capacity and lead to a decrease in actomyosin-generated tension and cell forces/stiffness.

Supplemental Materials

Molecular Biology of the Cell

Broussard et al.

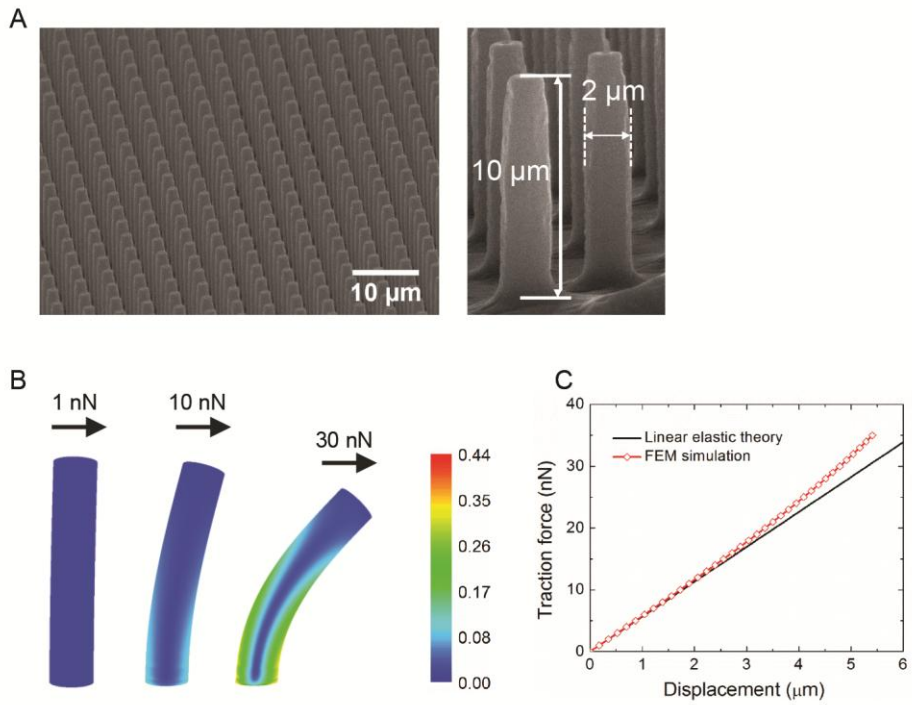

Supplemental Figure 1. (A) Representative SEM images of the MA. Pillars are orthogonally patterned with a height of 10 µm and a diameter of 2 µm. (B) Finite element simulations of pillar deflection under various traction levels. (C) The traction-displacement relationship begins to deviate from linear elastic theory as pillars undergo large deformation (>2.5 µm).

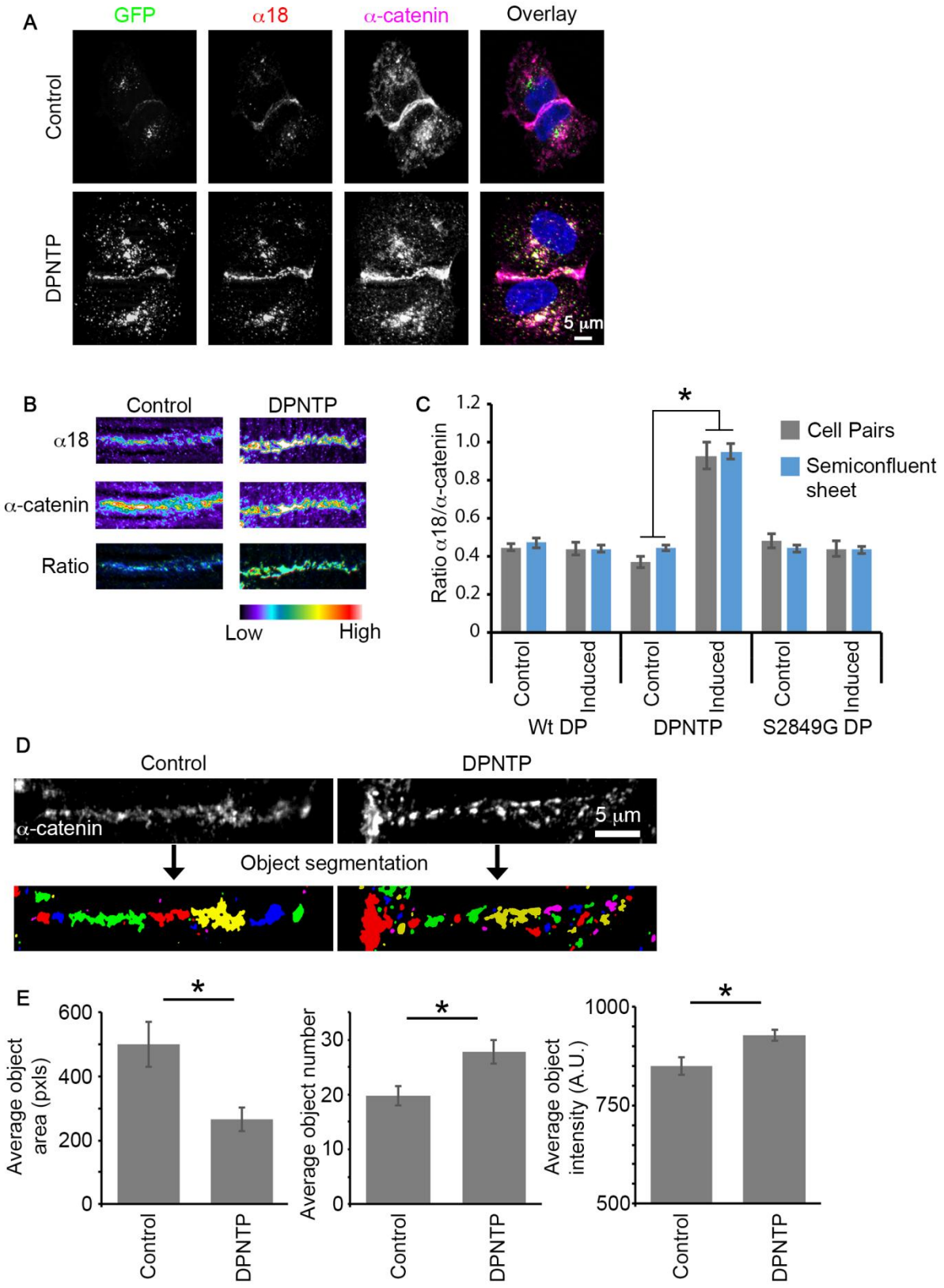

Supplemental Figure 2. (A) Apotome micrographs of a control (uninduced) and induced A431 cell pair expressing GFP-DPNTP and stained with the tension sensitive α-catenin (α18) antibody and total α-catenin are shown. Dapi indicates nuclei in blue. (B) Cell-cell border staining of α18 and total α-catenin as well as ratio images of α18 to total α-catenin in a control (uninduced) and induced A431

cell pair expressing GFP-DPNTP are shown in a pseudocolor scale in which cool colors represent relatively low values while warm colors represent relatively high values. (C) Quantification of the average cell-cell border intensity ratio of α18 to total α-catenin for control (uninduced) and induced cell pairs and semiconfluent (80%) cell sheets expressing the indicated DP variants are shown. Error bars represent the standard error of the mean from at least 14 cell pairs and 43 cell-cell junctions in the semiconfluent cell sheet from 3 independent experiments. *p<0.0001. (D) Upper, representative apotome micrographs of the cell-cell interface of control (uninduced) and induced A431 cells expressing GFP-DPNTP and immunostained with an α-catenin antibody are shown. Lower, images were thresholded and object segmentation was performed using MetaMorph Software. Colors represent individual objects segmented from the above fluorescence images. (E) The average object area, number of objects per cell-cell interface, and average α-catenin intensity per segmented object are shown for control (uninduced) and induced A431 cells expressing GFP-DPNTP. Error bars represent the standard error of the mean from at least 32 cells from 3 independent experiments. *p≤0.004.

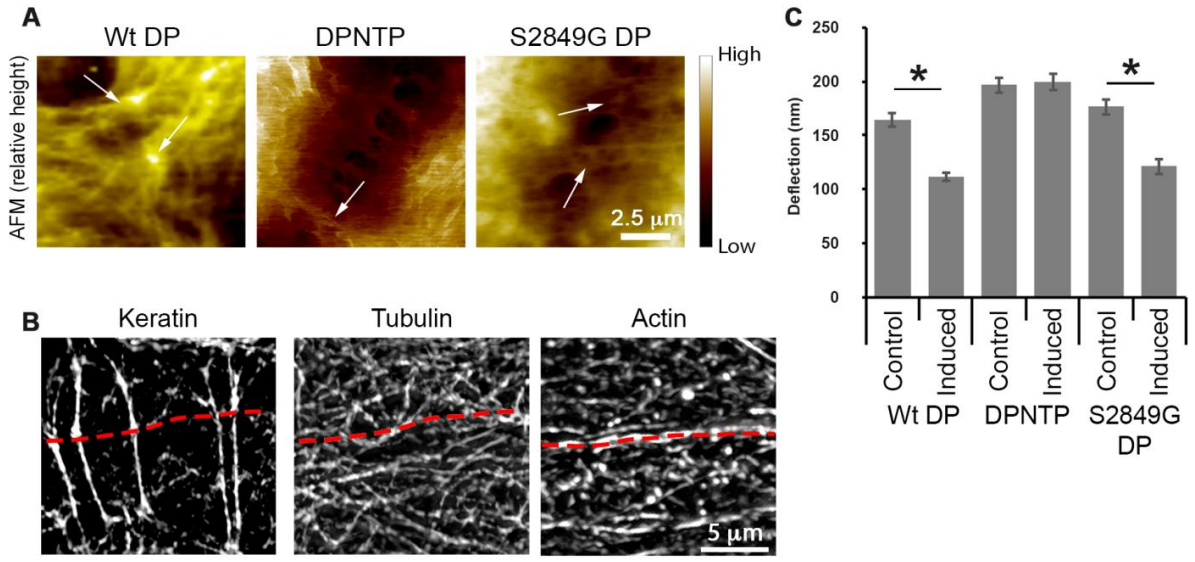

Supplemental Figure 3. (A) Representative AFM height images at cell-cell junctions of pairs of induced A431 cells expressing the indicated DP variants are shown. Images were contrasted to highlight the cytoskeletal bundles attached at cell-cell contacts (arrows). (B) Representative super-resolution images at the cell-cell interface (red dashed line) of control cells immunostained for the indicated cytoskeletal networks (keratin 18, Keratin; α-tubulin, Tubulin; and phalloidin, Actin) are shown. (C) Quantification of the average deflection of individual cytoskeletal bundles at cell junctions in control (uninduced) or induced A431 cells expressing the indicated DP variants as determined using AFM with a load up to 0.5 nN is shown. Error bars represent the standard error of the mean from at least 10 cells from 3 independent experiments. *p<0.05.

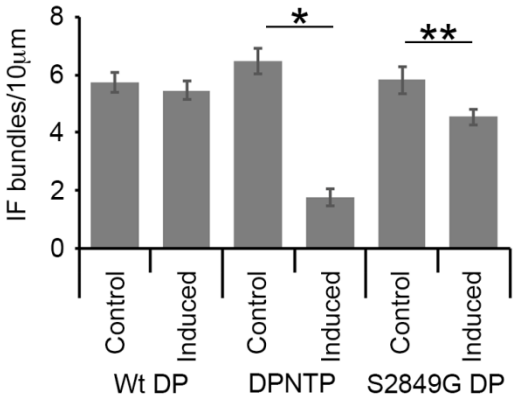

Supplemental Figure 4. Quantification of the number of IF bundles detected by immunofluorescence analysis of keratin staining entering sites of cell-cell contact in uninduced (control) and induced semiconfluent sheets of A431 cell lines expressing the indicated DP variants is shown. Error bars represent the standard error of the mean from at least 26 cells from 3 independent experiments. *$p<0.0001$, **$p=0.008$.